ACS APPLIED MATERIALS & INTERFACES

Research Article

www.acsami.org

Surface Modification of $MnFe_2O_4$ Nanoparticles to Impart Intrinsic Multiple Fluorescence and Novel Photocatalytic Properties

Monalisa Pal,* Rupali Rakshit, and Kalyan Mandal

Department of Condensed Matter Physics and Material Sciences, S. N. Bose National Centre for Basic Sciences, Block JD, Sector III, Salt Lake, Kolkata 700 098, India

Supporting Information

ABSTRACT: The $MnFe_2O_4$ nanoparticle has been among the most frequently chosen systems due to its diverse applications in the fields ranging from medical diagnostics to magnetic hyperthermia and site-specific drug delivery. Although numerous efforts have been directed in the synthesis of monodisperse $MnFe_2O_4$ nanocrystals, unfortunately, however, studies regarding the tuning of surface property of the synthesized nanocrystals through functionalization are sparse in the existing literature. Herein, we demonstrate the emergence of intrinsic multicolor fluorescence in $MnFe_2O_4$ nanoparticles from blue, cyan, and green to red, upon functionalization and further surface modification with a small organic ligand, Na-tartrate. Moreover, we have found an unprecedented photocatalytic property of the functionalized $MnFe_2O_4$ nanoparticles in the degradation of a model water contaminant. Detailed characterization through XRD, TEM, and FTIR confirms the very small size and functionalization of $MnFe_2O_4$ nanoparticles with a biocompatible ligand. Proper investigation through UV−visible absorption, steady-state and time-resolved photoluminescence study reveals that ligand-to-metal charge-transfer transition from the tartrate ligand to the lowest unoccupied energy level of $Mn^{2+/3+}$or Fe^{3+} of the NPs and Jahn−Teller distorted d−d transitions centered over Mn^{3+} ions in the NPs play the key role behind the generation of multiple fluorescence from the ligand-functionalized $MnFe_2O_4$ nanoparticles. VSM measurements indicates that the superparamagnetic nature of $MnFe_2O_4$ nanoparticles remains unchanged even after surface modification. We believe that the developed superparamagnetic, multicolor fluorescent $MnFe_2O_4$ nanopaticles would open up new opportunities as well as enhance their beneficial activities toward diverse applications.

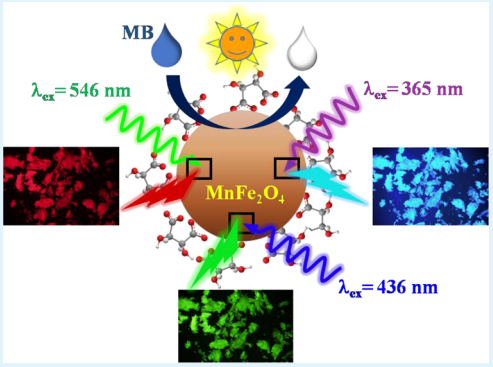

KEYWORDS: *$MnFe_2O_4$ nanoparticles, solubilization in aqueous medium, surface modification, emergence of multiple fluorescence, photocatalytic activity*

1. INTRODUCTION

Development of multifunctional nanoparticles for their advanced application in the field of biomedical diagnosis and therapy has been a key topic in the past decade and resulted in a progressive development of a new emerging research area called nanobiotechnology. The role of properly functionalized magnetic nanoparticles (MNPs) possesses several advantages that give rise to many exciting opportunities in the field of biomedical application.[1] The size tunability of MNPs from a few nanometers to tens of nanometers enables them to match with that of the biomolecules and effectively enhances their interaction possibility with different biological entities. Rationally surface-modified and highly water-dispersible MNPs that can be manipulated using an external magnetic field for targeting to a specific site, facilitate the enhancement of the MRI contrast and fluorescence imaging[2−5] for noninvasive diagnosis of morphology and function of healthy and ailing soft tissues in vivo, and AC magnetic-field-assisted hyperthermia treatment of cancer.[6] Very recently, significant attention has also been directed toward the development of MNPs as sustainable nanocatalysts for specific chemical transformations having both economic and environmental significance, considering their efficient activity, low cost, simple preparation method, high stability, and controlled separation by an external magnetic field.[7−11]

Generally, there are two conventional methods for the preparation of fluorescent magnetic nanoparticles, such as (i) functionalization of MNPs with fluorescent organic dyes[12] or polymers[3] and (ii) making nanocomposites with quantum dots.[4,5] The combined drawbacks of small photostability along with reduced quantum yields at near-infrared (NIR) wavelengths hamper the use of organic dyes for NIR-wavelength fluorescence imaging applications. On the other hand, inherent toxicity of QDs imposes serious limitation to their biomedical applications.[13] So, to improve the efficiency of the MNPs for biomedical applications, the development of biocompatible MNPs having intrinsic fluorescence property and photostability is highly desirable. Among the MNPs, extensive studies on iron

Received: December 24, 2013
Accepted: March 12, 2014
Published: March 12, 2014

   dx.doi.org/10.1021/am405950q | ACS Appl. Mater. Interfaces 2014, 6, 4903−4910

oxide and ferrite nanoparticles have been performed due to their excellent superparamagnetic behavior and chemical stability. Particularly, among the ferrites, research on $MnFe_2O_4$ has been a key topic because of its highest magnetization which enables it potentially useful as MRI contrast agents and magnetic probes capable of being manipulated under an external magnetic field.[14−18] Recently, significant efforts have also been given for the development of $MnFe_2O_4$ NPs as targeted multimodal imaging agents, upon conjugating fluorescent dye molecules and cancer cell surface receptors with the NPs' surface.[3,19,20] However, despite recent advancement, aqueous phase insolubility and the absence of any inherent optical properties of the NPs possess a huge concern for their direct biomedical applications. Thus, the designing of an appropriate surface modification and functionalization strategy is highly desirable to expedite the diverse biological applicability of the NPs.

Herein, we report the development of $MnFe_2O_4$ as a multifunctional nanoprobe having intrinsic multicolor fluorescence, superparamagnetism, and novel photocatalytic activity. We have synthesized 4−5 nm sized $MnFe_2O_4$ nanoparticles following a wet chemical method previously reported by Sun et al., with slight modification.[21] We have used the reactivity of tartrate ligands to solubilize the as-prepared NPs into the aqueous environment. Employing a further surface modification approach, we have observed the emergence of multicolor fluorescence (starting from blue, cyan, green to red) from the water-soluble tartrate-functionalized $MnFe_2O_4$ NPs (T-$MnFe_2O_4$ NPs). To investigate the mechanistic origin of this novel multicolor fluorescence property, we have used several spectroscopic techniques. It has been found that the ligand-to-metal charge-transfer (LMCT) transitions from the tartrate ligand to the lowest unoccupied energy level of $Mn^{2+/3+}$ or Fe^{3+} metal ions in the NPs and Jahn−Teller (J-T) distorted d−d transitions centered over Mn^{3+} ions play the key role. Finally, we intended to exploit the photoexcitation (UV−vis) behavior of the T-$MnFe_2O_4$ NPs in catalysis. It has been found that the T-$MnFe_2O_4$ NPs exhibit unprecedented photocatalytic property in the degradation of methylene blue (MB), an organic dye used in textile industries and a model water contaminant.

2. EXPERIMENTAL SECTION

2.1. Material Used. Fe(III)acetylacetonate, oleylamine, methylene blue (MB), 2-amino-purine (2AP), 4′,6-diamidino-2-phenylindole (DAPI), Hoechst 33258, and Rhodamine B (RhB) were obtained from Sigma-Aldrich. Mn(II)acetate, diphenyl ether, oleic acid, and cetyl alcohol were received from Loba Chemie. Tartaric acid, sodium hydroxide (NaOH), and potassium bromide were purchased from Merck. All the reagents are analytical grade and used without further purification.

2.2. Synthesis Procedure and Functionalization of $MnFe_2O_4$ NPs. $MnFe_2O_4$ NPs were synthesized by a template-free wet chemical process following a previous report with some modification,[21] which involves the high-temperature (260 °C) reflux of $Mn(ac)_2$ and $Fe(acac)_3$ in diphenyl ether in the presence of oleic acid, oleylamine, and cetyl alcohol. As-prepared $MnFe_2O_4$ NPs were cyclomixed with 0.5 M Na-tartrate solution (prepared in Milli-Q water and pH of the solution was made ∼ 7) for 12 h at room temperature. The nonfunctionalized larger $MnFe_2O_4$ NPs were filtered out with a syringe filter of 0.22 μm in diameter. The as-obtained pale yellow colored filtrate was tartrate-functionalized $MnFe_2O_4$ nanoparticles (T-$MnFe_2O_4$ NPs). To induce the multicolor fluorescence property, T-$MnFe_2O_4$ NPs were heated at about 70 °C for 8 h under extensive stirring condition after maintaining the pH of the solution at ∼12 with dropwise addition of NaOH solution. After this high pH and temperature treatment, the color of the solution turned to brownish and showed intense fluorescence under UV light (inset of Figure 3a). To prepare the solid powdered samples required for magnetic study (vibrating sample magnetometry, VSM) and Fourier transform infrared (FTIR) spectroscopic measurements, we dialyzed T-$MnFe_2O_4$ NPs solution (to remove excess ligands) and lyophilized it, followed by drying over a water bath.

2.3. Characterization Techniques. XRD patterns were obtained by employing a scanning rate of 0.02° s^{-1} in the 2θ range from 20° to 80° by a Rigaku miniflex II diffractometer equipped with Cu Kα radiation (at 40 mA and 40 kV).

For TEM study, samples were prepared by drop-casting T-$MnFe_2O_4$ NPs solution on a 300-mesh carbon-coated copper grid and dried overnight in air. Particle size was determined from TEM micrographs, and elemental analysis was performed from the EDX spectrum recorded by an FEI Tecnai TF-20 field emission high-resolution transmission electron microscope operating at 200 kV.

UV−vis absorbance spectra of the T-$MnFe_2O_4$ NPs were recorded with a Shimadzu model UV-2600 spectrophotometer using a quartz cuvette of 1 cm path length. Steady-state fluorescence emission and excitation spectra of T-$MnFe_2O_4$ NPs were recorded on a Horiba Jobin Yvon Model Fluorolog fluorimeter. Fluorescence micrographs of as-prepared and functionalized $MnFe_2O_4$ NPs were captured using an Olympus BX61 Fluorescence microscope employing 365, 436, and 546 nm excitation wavelengths.

Time-resolved fluorescence transients of T-$MnFe_2O_4$ NPs were recorded using a picosecond pulsed diode laser (nano LED from HORIBA JOBIN YVON) based TCSPC fluorescence spectrometer, against excitation at 377 and 295 nm, employing MCP-PMT as a detector. The emitted light from T-$MnFe_2O_4$ NPs solution was collected at a right angle to the direction of the excitation beam maintaining magic-angle polarization (54.7°) with a band pass of 2 nm. For the 377 nm laser source, the full width at half-maximum (FWHM) of the instrument response function was 270 ps, and the resolution was 28 ps per channel. In the case of 295 nm excitation, the pulse duration was <1 ns. The data were fitted to multiexponential functions after deconvolution of the instrument response function by an iterative reconvolution technique using IBH DAS 6.2 data analysis software in which reduced χ^2 and weighted residuals serve as parameters for goodness of fit. All the optical studies were performed at room temperature (298 K).

FTIR studies were performed by a JASCO FTIR-6300 spectrometer, to ensure the attachment and interaction of the tartrate molecules with $MnFe_2O_4$ NPs. For FTIR measurements, pellets were prepared after homogeneous mixing of lyophilized powdered samples with KBr. The background was corrected by a reference of KBr pellets.

Magnetic study was carried out in a Lake Shore VSM equipped with an electromagnet, capable of generating a field of up to 1.6 T at 300 K.

For the study of photocatalysis, we used an 8 W UV lamp as the UV light source and a 100 W incandescent bulb (its optical spectra exactly mimic sunlight having a continuum throughout the visible region) as the visible light source, from Philips. A 1:1 (4.6 μM each) aqueous solution of MB and T-$MnFe_2O_4$ NPs was homogeneously mixed for 1 h in a quartz cuvette in the dark, maintaining the pH of the solution at ∼3. Then the cuvette was placed ∼2 cm apart from the light source and the absorbance of MB in the reaction mixture was measured time to time by the UV−vis spectrophotometer.

3. RESULTS AND DISCUSSION

$MnFe_2O_4$ NPs used for ligand functionalization were prepared through high-temperature decomposition of the metal acetate and acetylacetonate precursors. TEM study has been carried out to evaluate the morphology and monodispersity of both the as-prepared $MnFe_2O_4$ NPs and highly water-soluble T-$MnFe_2O_4$ NPs, in detail. As shown in Figure 1a, as-prepared $MnFe_2O_4$ NPs have a nearly homogeneous size distribution (3.5−7 nm) with an average diameter of 4.80 ± 0.16 nm

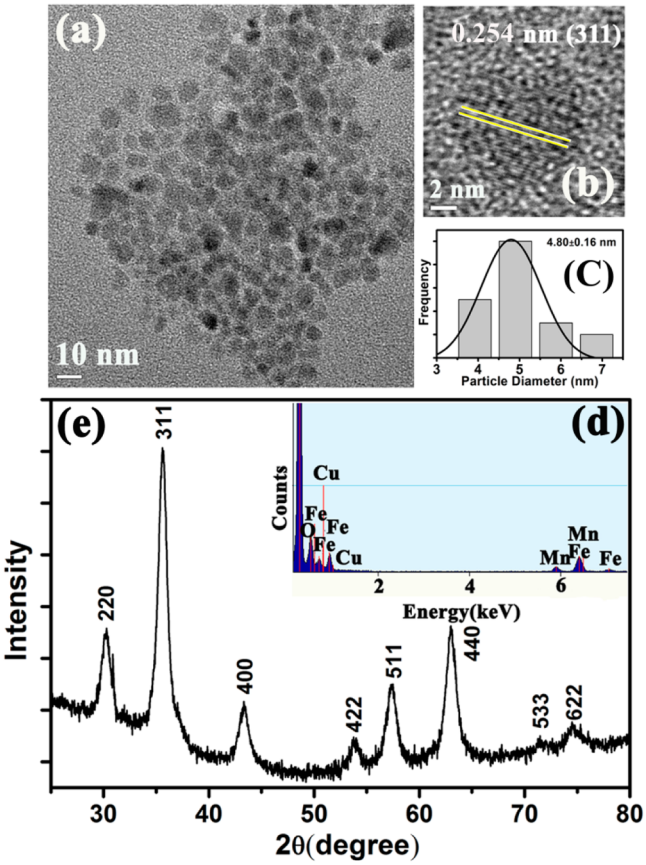

Figure 1. (a) TEM image of the as-prepared bare $MnFe_2O_4$ NPs. (b) Corresponding HRTEM image indicates high crystallinity and shows lattice fringes. (c) Size distribution of as-prepared $MnFe_2O_4$ NPs. (d) EDX spectrum of the NPs indicating the presence of Mn, Fe, and O. (e) XRD pattern of as-prepared $MnFe_2O_4$ NPs. All diffraction peaks in the figure are perfectly indexed in the literature to the cubic spinel structure of $MnFe_2O_4$ NPs.

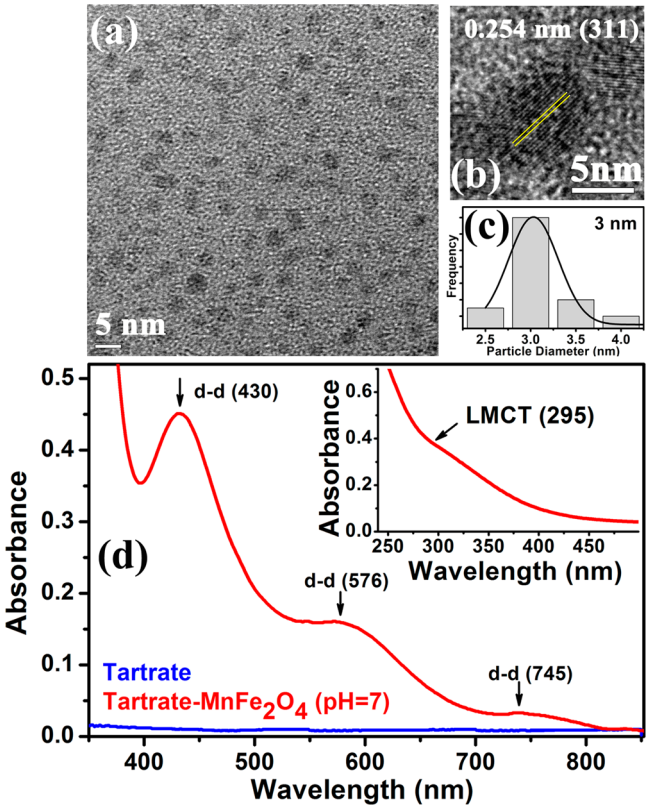

Figure 2. (a) TEM image of highly dispersible T-$MnFe_2O_4$ NPs in aqueous medium. (b) Lattice fringes in the corresponding HRTEM image, indicating high crystalline nature of the NPs. (c) Size distribution of T-$MnFe_2O_4$ NPs. (d) UV–vis absorption spectrum for T-$MnFe_2O_4$ NPs and Na-tartrate at pH ∼ 7. Inset shows higher energy strong absorption band due to LMCT transitions for very dilute T-$MnFe_2O_4$ NPs solution.

(Figure 1c) and most of the NPs have been found to be spherical in shape. The corresponding HRTEM image (Figure 1b) confirms the crystallinity of the NPs. The calculated interplanar distance between the lattice fringes is about 0.254 nm, which corresponds to the distance between (311) planes of the $MnFe_2O_4$ crystal lattice. Energy-dispersive X-ray (EDX) spectroscopic analysis of $MnFe_2O_4$ NPs (Figure 1d) confirms the elemental composition of only manganese, iron, and oxygen. Figure 1e shows the XRD pattern of as-prepared $MnFe_2O_4$ NPs. All the diffraction peaks in the figure perfectly match with the cubic spinel structure of $MnFe_2O_4$ NPs as reported in the literature.[21]

To study the effect of surface functionalization on the properties of $MnFe_2O_4$ NPs, we have functionalized the as-prepared $MnFe_2O_4$ NPs with tartrate ligands. Figure 2a shows the TEM image of T-$MnFe_2O_4$ NPs having a spherical shape with an average diameter of ∼3 nm (Figure 2c). From the HRTEM image of T-$MnFe_2O_4$ NPs (shown in Figure 2b), the highly crystalline nature of the NPs is clearly evident. The calculated interplanar distance between the fringes has been found to be 0.254 nm corresponding to the (311) plane of the crystal lattice. As shown in Figure 2d, T-$MnFe_2O_4$ NPs (at pH ∼ 7) exhibit a distinct absorption pattern in the UV–vis region, indicating a significant variation of the surface electronic structure of the NPs upon functionalization with the tartrate ligand. The observed peak at 295 nm, having relatively higher absorbance (shown in the inset), can be attributed to ligand-to-metal charge-transfer (LMCT) transitions involving the interaction between the highest occupied energy level of tartrate and the lowest unoccupied energy levels of Mn^{2+}/Mn^{3+}/Fe^{3+} metal ion centers on the NPs' surface.[22] Additional three peaks with gradually decreasing intensities and increasing broadness, observed around 430, 576, and 745 nm, can be due to the possible d–d transitions involving $Mn^{2+/3+}$ or Fe^{3+} ions in the T-$MnFe_2O_4$ NPs' surface. (Although Mn in the 3+ oxidation state was not supposed to be present in the $MnFe_2O_4$ NPs, however, due to the strong pH dependence of oxidation states of Mn, upon solubilization of the nanoparticles into the aqueous environment at pH ∼ 7, formation of Mn^{3+} states is highly probable.)[23,24] We can safely discard the possibility of d–d transitions in the case of both Fe^{3+} (d^5) and Mn^{2+} (d^5) ions, as in both cases, this transition is forbidden (both Laporte and spin-forbidden) according to the selection rule of fundamental atomic spectroscopy.[25] However, in the case of Mn^{3+} (d^4), the degeneracy of t_{2g} and e_g levels could be lost due to Jahn–Teller (J-T) distortion in the high-spin octahedral environment. In terms of spectroscopic term symbols, we can explain the generation of three bands (430, 576, and 745 nm) due to the transitions of $5B_{1g} \rightarrow 5E_g$, $5B_{1g} \rightarrow 5B_{2g}$, and $5B_{1g} \rightarrow 5A_{1g}$, respectively.[26,27] Interestingly, when we excited T-$MnFe_2O_4$ NPs (pH ∼ 7) at these different UV–vis absorption peak/band positions, we found multiple fluorescence.

dx.doi.org/10.1021/am405950q | ACS Appl. Mater. Interfaces 2014, 6, 4903–4910

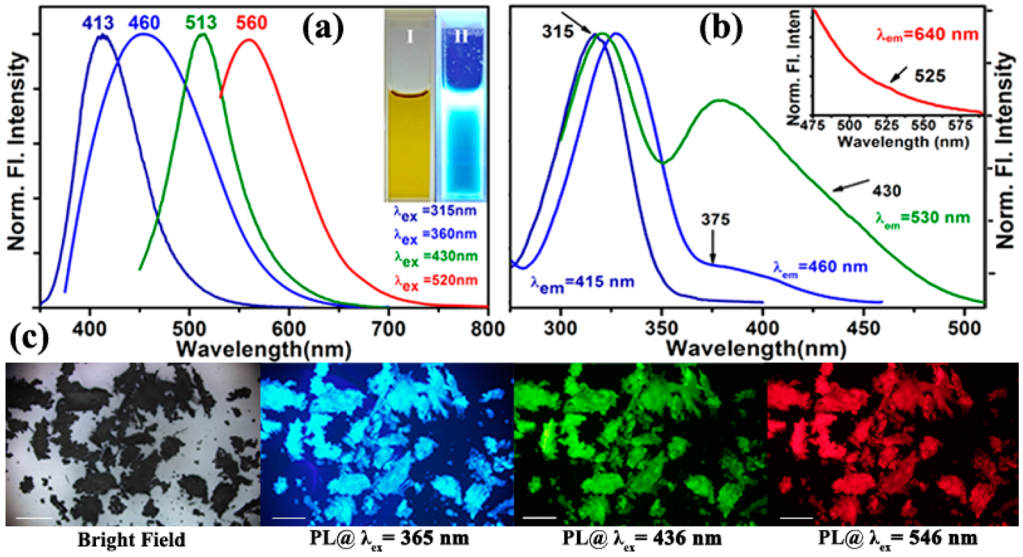

Figure 3. (a) Normalized steady-state fluorescence emission spectra collected from T-$MnFe_2O_4$ NPs with four different excitation wavelengths of 315, 360, 430, and 520 nm. I and II in the inset show the photographs of aqueous T-$MnFe_2O_4$ NPs solution under visible and UV light, respectively. (b) Fluorescence excitation spectra of T-$MnFe_2O_4$ NPs at different emission maxima of 415, 460, 530, and 640 nm. (c) Fluorescence micrographs of T-$MnFe_2O_4$ NPs powder under bright-field, UV (365 nm), blue (436 nm), and green (546 nm) light irradiation. The scale bars in all the images are 500 μm.

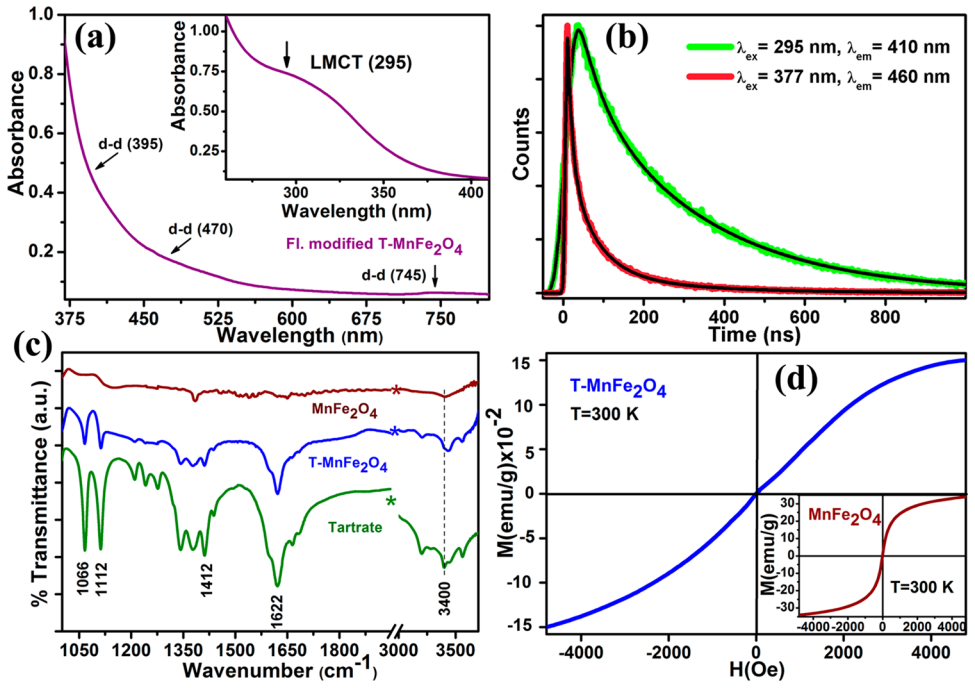

Figure 4. (a) UV–vis absorption spectrum for fluorescence-modified T-$MnFe_2O_4$ NPs at pH ~ 12. (b) Picosecond-resolved fluorescence transients of T-$MnFe_2O_4$ NPs studied at emission wavelengths of 410 and 460 nm upon excitation with laser sources of 295 and 377 nm wavelengths, respectively. (c) FTIR spectra of as-prepared $MnFe_2O_4$ and T-$MnFe_2O_4$ NPs along with Na-tartrate alone. (d) Plot of magnetization versus applied magnetic field (M–H) for T-$MnFe_2O_4$ NPs at 300 K. Inset shows M–H plot for as-prepared $MnFe_2O_4$ NPs at 300 K.

Although, the fluorescence observed upon excitation of the sample at the LMCT band (295 nm) was very strong, fluorescence from d–d excited states (J-T distorted states) was found to be considerably weak. So, to make the d–d excited states highly fluorescent, the pH of the as-prepared T-$MnFe_2O_4$ NPs was adjusted to ~12 (to convert all the Mn ions into +3 oxidation state),[24] by dropwise addition of NaOH solution, followed by heat treatment at 70 °C for 8 h. This further surface modification step significantly enhanced the fluorescence intensity from d–d (J-T distorted) as well as from LMCT excited states. Figure 3a shows the normalized multiple fluorescence spectra of T-$MnFe_2O_4$ NPs (pH ~ 12) having emission maxima at 413, 460, 513, and 560 nm, covering the whole visible region from blue, cyan, green to red, against excitation at 315, 360, 430, and 520 nm, respectively. Nice correlation between the corresponding excitation spectrum of different emission maximum, as shown in Figure 3b, and UV–vis absorption spectra of fluorescence-modified T-$MnFe_2O_4$

dx.doi.org/10.1021/am405950q | ACS Appl. Mater. Interfaces 2014, 6, 4903–4910

Table 1. Lifetime Values of Picosecond Time-Resolved Fluorescence Transients of T-$MnFe_2O_4$ NPs, Detected at Fluorescence Maxima 410 and 460 nm upon Excitation at 295 and 377 nm Wavelengths, Respectively[a]

system	excitation wavelength, λ_{ex} (nm)	fluorescence peak, λ_{em} (nm)	τ_1 (ns)	τ_2 (ns)	τ_3 (ns)	τ_{av} (ns)
T-$MnFe_2O_4$ NPs	295	410	1.46 (35.32)	8.58 (64.68)		6.06
	377	460	1.88 (34.06)	7.14 (6.23)	0.31 (59.71)	1.27

[a]The relative weight percentages of the time components are shown in parentheses.

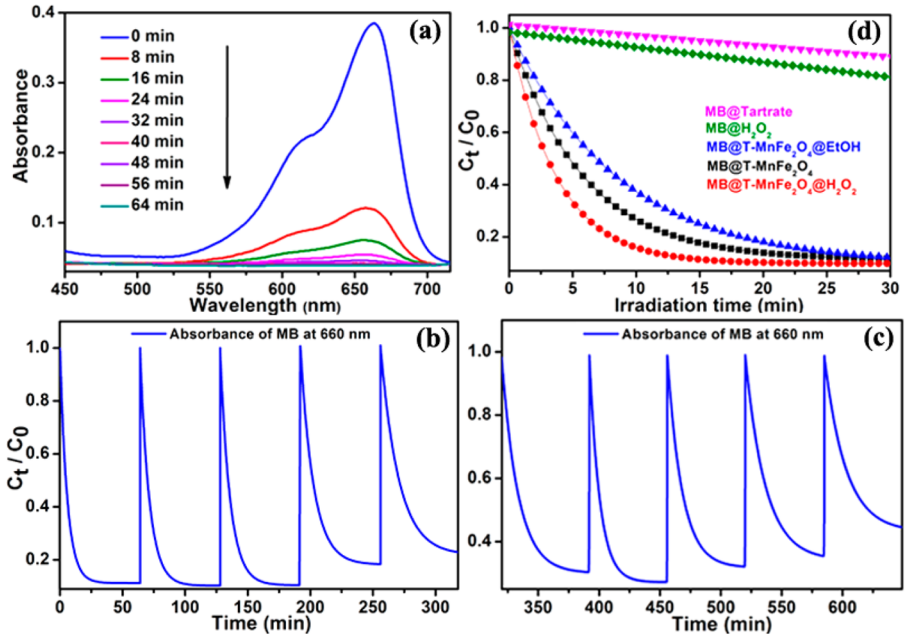

Figure 5. (a) UV–vis spectral changes of aqueous solution of methylene blue (MB) in the presence of T-$MnFe_2O_4$ NPs with time, under UV irradiation. (b, c) Show the plots of relative concentration of MB monitored at 660 nm versus time for 10 consecutive cycles, showing reusability of T-$MnFe_2O_4$ in MB degradation under UV light. (d) Shows the rate of photocatalytic degradation of MB (monitored at 660 nm) under UV radiation in the presence of Na-tartrate, H_2O_2, T-$MnFe_2O_4$ NPs, T-$MnFe_2O_4$ NPs @EtOH, and T-$MnFe_2O_4$ NPs @H_2O_2.

NPs (Figure 4a), further substantiate the exact excitation positions of the respective fluorescence emissions. Photographs of the aqueous solution of T-$MnFe_2O_4$ NPs under visible and UV light are shown in the inset of Figure 3a. The amazing fluorescence micrographs of T-$MnFe_2O_4$ NPs powder, as shown in Figure 3c, demonstrate that the black powder of T-$MnFe_2O_4$ NPs under bright field gives rise to fluorescent colors like cyan, green, and red upon excitation at 365, 436, and 546 nm, respectively, by using proper filters. Figure S1 (Supporting Information) shows that the fluorescence microscopic images of as-prepared bare $MnFe_2O_4$ NPs under identical conditions have no such fluorescence. Fluorescence quantum yields (QYs) of the T-$MnFe_2O_4$ NPs have been calculated by following the relative method of Williams et al.,[28] which involves the use of well-characterized standard fluorescent compounds with known QY values. Fluorescence QYs of 11.83% (for 413 nm band), 2.4% (for 460 nm band), 2% (for 513 nm band), and 0.14% (for 560 nm band) were obtained relative to the standard fluorescent compounds, such as 2-aminopurine (2AP), 4′,6-diamidino-2-phenylindole (DAPI), Hoechst 33258, and Rhodamine B (RhB), respectively. Thus, the emergence of multicolor fluorescence in $MnFe_2O_4$ NPs was induced by tartrate functionalization and then reinforced by further surface modification.

To get deeper mechanistic insight into the appearance of multiple fluorescence, we have carried out picosecond-resolved fluorescence decay transient measurements of T-$MnFe_2O_4$ NPs employing the TCSPC technique. Figure 4b represents the time-resolved fluorescence decay transients of T-$MnFe_2O_4$ NPs at two different fluorescence maxima of 410 and 460 nm using two different pulsed diode laser excitation sources of 295 and 377 nm wavelengths, respectively. As evident from the figure, the significantly larger average excited-state lifetime (τ) of T-$MnFe_2O_4$ NPs observed for the 410 nm fluorescence band (6.06 ns) compared to that for the 460 nm fluorescence band (1.27 ns) strongly suggests a mechanistic difference in the origin of these two fluorescence bands. The lifetime components and their corresponding weight percentages are found in Table 1. With this fluorescence lifetime study, the proposition regarding the origin of this multiple fluorescence made from steady-state experiments is reconfirmed and we reasonably conclude that the LMCT excited state is responsible for the 410 nm fluorescence, whereas the 460 nm fluorescence is attributed to the J-T distorted d–d transition. It is quite obvious that the other two lower energy fluorescences at 513 and 560 nm would also correspond to other probable d–d transitions.

To obtain definite evidence for the involvement of Mn^{3+} ions in the generation of multiple fluorescence, we have studied the pH dependency of the fluorescence intensity. At acidic/neutral pH, Mn^{3+} ions are unstable and tend to disproportionate into Mn^{2+} and Mn^{4+}, whereas, in alkaline pH, comproportionation of Mn^{2+} and Mn^{4+} to Mn^{3+} ions takes place.[24,29] We have monitored the fluorescence intensity of T-$MnFe_2O_4$ NPs at 413 and 460 nm (against excitation at 315 and 360 nm, respectively), upon decreasing the pH of the NPs solution

from 12 to 3. Gradual reduction of fluorescence intensity with decreasing pH is clearly evident from Figure S2 (Supporting Information), which further corroborates our conclusion that both the LMCT and the d−d transitions (J-T distorted) are associated with Mn^{3+} ions on the NPs' surface.

To confirm the attachment of tartrate ligands to the nanoparticle surface, a comparative FTIR spectroscopic study was performed on bare and T-$MnFe_2O_4$ NPs along with Na-tartrate alone (Figure 4c). As shown in the figure, in the case of tartrate, two sharp peaks arising at 1066 and 1112 cm^{-1} are due to the C−OH stretching modes,[30] and peaks at 1412 and 1622 cm^{-1} are attributed to symmetric and asymmetric stretching modes of the carboxylate groups (COO^-) of tartrate, respectively.[31] Upon interaction with the nanoparticle surface, i.e., in the case of T-$MnFe_2O_4$, all these different bands are perturbed significantly along with the band at 3400 cm^{-1} corresponding to the stretching vibrational modes of the hydroxyl group (O−H),[30] which clearly indicates the involvement of both $-COO^-$ and −OH groups in the functionalization process.

To study the magnetic behavior of $MnFe_2O_4$ NPs before and after functionalization with tartrate ligands, we have investigated applied-field-dependent magnetization measurements ($M-H$) for both the samples using VSM. The superparamagnetic nature of as-prepared bare $MnFe_2O_4$ NPs is evident from the inset of Figure 4d. In the case of T-$MnFe_2O_4$ NPs also, this superparamagnetic nature remains unchanged (evident from Figure 4d), although, with a decrease in saturation magnetization, which could be due to the presence of a diamagnetic ligand coating around the NPs after functionalization.

Having developed $MnFe_2O_4$ NPs as multiple fluorescent material, we sought to exploit their broad optical excitation (absorption) throughout the UV−vis region, for photocatalysis. In our study, as an analyte, we have used methylene blue (MB), which is a model water contaminant. Figure 5 demonstrates the unprecedented photocatalytic efficiency of T-$MnFe_2O_4$ NPs in MB degradation under UV light irradiation. Figure 5a shows the full absorption spectra of MB in the presence of T-$MnFe_2O_4$ NPs with time, under UV irradiation at pH ∼ 3. We have found that the photoinduced discoloration of MB in the presence of T-$MnFe_2O_4$ NPs takes place exponentially with time following the first-order rate equation with a kinetic rate constant (k) of 17.46 × 10^{-2} min^{-1}, and a total photodegradation of 70% takes place within the first 8 min and 90% occurs within 40 min of UV irradiation. To ensure that the catalyst could be recycled without any significant loss of activity, we started the experiment with 1:1 (4.6:4.6 μM) MB/catalyst for the first cycle, and after every 64 min, we added the same dose of MB (4.6 μM) into the reaction mixture up to 10 doses. Keeping the catalyst concentration fixed at 4.6 μM (without addition of extra catalyst after the 1st cycle), MB decomposition kinetics of different cycles was studied by monitoring the decrease of MB absorbance at 660 nm using UV−vis spectroscopy. Figure 5b,c demonstrates the plots of relative concentration of MB versus time, up to 10 consecutive cycles, revealing the reusability of T-$MnFe_2O_4$ NPs catalyst with an almost unchanged degradation rate. To investigate whether the catalytic process is associated with a radical pathway, we have performed the MB degradation study (as shown in Figure 5d) in the presence of a radical initiator (H_2O_2, a source of •OH radicals) and a radical scavenger (EtOH, ethanol), separately. Figure 5d shows the comparative study of MB degradation rate in the presence of Na-tartrate (as blank experiment), H_2O_2, T-$MnFe_2O_4$ NPs, T-$MnFe_2O_4$ NPs @EtOH, and T-$MnFe_2O_4$ NPs @H_2O_2. It has been observed that, upon addition of a radical scavanger, the rate of MB degradation decreases effectively (k = 11.82 × 10^{-2} min^{-1}), whereas, with addition of a very small concentration (156 nM) of H_2O_2, the photodegradation rate increases considerably (k = 26.85 × 10^{-2} min^{-1}). As anticipated, in the presence of only tartrate or H_2O_2, the degradation takes place negligibly. The above study confirms that the photodegradation follows a radical pathway involving reactive oxygen species (ROS). We propose that, due to the very small size of T-$MnFe_2O_4$ NPs and negatively charged surface ligands (tartrate), MB molecules (cationic dye) get the opportunity for greater interaction with the NPs, which ultimately leads to efficient catalytic degradation. Additionally, we have also checked the catalytic efficiency of the NPs toward MB degradation, in the presence of visible light activation (as shown in Figure 6). Interestingly,

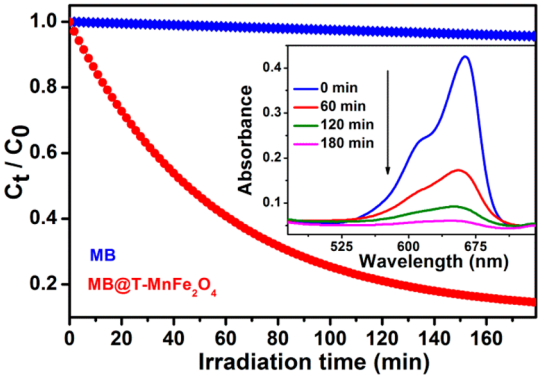

Figure 6. Shows the rate of photocatalytic degradation of MB (monitored at 660 nm) in the absence and presence of T-$MnFe_2O_4$ NPs under visible light. Inset shows the full absorption spectra of methylene blue (MB) in the presence of T-$MnFe_2O_4$ NPs with time, under visible light irradiation.

T-$MnFe_2O_4$ NPs show photocatalytic degradation of MB under visible light also, although, with a moderate rate (k = 1.83 × 10^{-2} min^{-1}). Relatively less photocatalytic efficiency of the NPs under visible light excitation can be attributed to the higher energy of UV light as compared to visible light as well as higher extinction coefficient of T-$MnFe_2O_4$ NPs in the UV region than its visible counterpart.

4. CONCLUSIONS

In summary, we have demonstrated a facile functionalization and further surface modification strategy for the development of $MnFe_2O_4$ NPs as a biocompatible novel multifunctional biological probe, simultaneously having superparamagnetism and inherent multicolor fluorescence covering the whole UV−vis region from blue, cyan, and green to red. Employing various spectroscopic techniques, we have investigated the exact mechanistic origin of the remarkable optical properties of $MnFe_2O_4$ NPs upon functionalization with tartrate. We believe that this novel functionalized material (T-$MnFe_2O_4$ NPs) might open up new opportunities to their prospective use in bioimaging, drug delivery, and other biomedical applications in the future, due to the coexistence of its biocompatibility, ligand-induced intrinsic multiple fluorescence, and superparamagnetism. Furthermore, we have also demonstrated the unprecedented photocatalytic activity of the functionalized material for

the degradation of a model water contaminant. Given the possibility of ligand-induced appearance of new magneto-fluorescence properties in the nanomaterials and excellent photocatalytic activity, we expect that this work will contribute significantly to the design and development of new materials for their advanced technological application.

■ ASSOCIATED CONTENT

Supporting Information

Supporting Information contains fluorescence micrographs of bare $MnFe_2O_4$ NPs under bright-field, UV, blue, and green light and pH-dependent study of fluorescence intensity. This material is available free of charge via the Internet at http://pubs.acs.org.

■ AUTHOR INFORMATION

Corresponding Author

*E-mail: monalisa.pal6@gmail.com, monalisa12@bose.res.in.

Notes

The authors declare no competing financial interest.

■ ACKNOWLEDGMENTS

We thank CSIR for financial grants. The authors would like to thank Mr. Mahesh Agarwal and Dr. Deepak Kumar Sinha from IACS, Kolkata, for providing the fluorescence microscopy facility used in this study. We thank Ms. Urmi Chakraborty, Mr. Samik Roy Moulik, and Mr. Dipankar Roy for performing XRD, TEM, and VSM measurements, respectively.

■ REFERENCES

(1) Reddy, L. H.; Arias, J. L.; Nicolas, J.; Couvreur, P. Magnetic Nanoparticles: Design and Characterization, Toxicity and Biocompatibility, Pharmaceutical and Biomedical Applications. *Chem. Rev.* **2012**, *112* (11), 5818−5878.

(2) Gao, J.; Liang, G.; Cheung, J. S.; Pan, Y.; Kuang, Y.; Zhao, F.; Zhang, B.; Zhang, X.; Wu, E. X.; Xu, B. Multifunctional Yolk−Shell Nanoparticles: A Potential MRI Contrast and Anticancer Agent. *J. Am. Chem. Soc.* **2008**, *130* (35), 11828−11833.

(3) Yang, J.; Lim, E.-K.; Lee, H. J.; Park, J.; Lee, S. C.; Lee, K.; Yoon, H.-G.; Suh, J.-S.; Huh, Y.-M.; Haam, S. Fluorescent Magnetic Nanohybrids as Multimodal Imaging Agents for Human Epithelial Cancer Detection. *Biomaterials* **2008**, *29* (16), 2548−2555.

(4) Gao, J.; Zhang, W.; Huang, P.; Zhang, B.; Zhang, X.; Xu, B. Intracellular Spatial Control of Fluorescent Magnetic Nanoparticles. *J. Am. Chem. Soc.* **2008**, *130* (12), 3710−3711.

(5) Kim, H.; Achermann, M.; Balet, L. P.; Hollingsworth, J. A.; Klimov, V. I. Synthesis and Characterization of Co/CdSe Core/Shell Nanocomposites: Bifunctional Magnetic-Optical Nanocrystals. *J. Am. Chem. Soc.* **2004**, *127* (2), 544−546.

(6) Johannsen, M.; Gneveckow, U.; Eckelt, L.; Feussner, A.; Waldofner, N.; Scholz, R.; Deger, S.; Wust, P.; Loening, S. A.; Jordan, A. Clinical Hyperthermia of Prostate Cancer Using Magnetic Nanoparticles: Presentation of a New Interstitial Technique. *Int. J. Hyperthermia* **2005**, *21* (7), 637−647.

(7) Gawande, M. B.; Rathi, A. K.; Nogueira, I. D.; Varma, R. S.; Branco, P. S. Magnetite-Supported Sulfonic Acid: A Retrievable Nanocatalyst for the Ritter Reaction and Multicomponent Reactions. *Green Chem.* **2013**, *15* (7), 1895−1899.

(8) Gawande, M. B.; Bonifacio, V. D. B.; Varma, R. S.; Nogueira, I. D.; Bundaleski, N.; Ghumman, C. A. A.; Teodoro, O. M. N. D.; Branco, P. S. Magnetically Recyclable Magnetite−Ceria (Nanocat-Fe-Ce) Nanocatalyst − Applications in Multicomponent Reactions Under Benign Conditions. *Green Chem.* **2013**, *15* (5), 1226−1231.

(9) Li, Y.; Tan, H.; Yang, X.-Y.; Goris, B.; Verbeeck, J.; Bals, S.; Colson, P.; Cloots, R.; Van Tendeloo, G.; Su, B.-L. Well Shaped Mn_3O_4 Nano-octahedra with Anomalous Magnetic Behavior and Enhanced Photodecomposition Properties. *Small* **2011**, *7* (4), 475−483.

(10) Zhang, P.; Zhan, Y.; Cai, B.; Hao, C.; Wang, J.; Liu, C.; Meng, Z.; Yin, Z.; Chen, Q. Shape-Controlled Synthesis of Mn_3O_4 Nanocrystals and their Catalysis of the Degradation of Methylene Blue. *Nano Res.* **2010**, *3* (4), 235−243.

(11) Gawande, M. B.; Branco, P. S.; Varma, R. S. Nano-magnetite (Fe_3O_4) as a Support for Recyclable Catalysts in the Development of Sustainable Methodologies. *Chem. Soc. Rev.* **2013**, *42* (8), 3371−3393.

(12) Gu, H.; Xu, K.; Yang, Z.; Chang, C. K.; Xu, B. Synthesis and Cellular Uptake of Porphyrin Decorated Iron Oxide Nanoparticles-A Potential Candidate for Bimodal Anticancer Therapy. *Chem. Commun.* **2005**, *34*, 4270−4272.

(13) Resch-Genger, U.; Grabolle, M.; Cavaliere-Jaricot, S.; Nitschke, R.; Nann, T. Quantum Dots Versus Organic Dyes as Fluorescent Labels. *Nat. Methods* **2008**, *5* (9), 763−775.

(14) Li, Z.; Wang, S. X.; Sun, Q.; Zhao, H. L.; Lei, H.; Lan, M. B.; Cheng, Z. X.; Wang, X. L.; Dou, S. X.; Lu, G. Q. Ultrasmall Manganese Ferrite Nanoparticles as Positive Contrast Agent for Magnetic Resonance Imaging. *Adv. Healthcare Mater.* **2013**, *2* (7), 958−964.

(15) Kim, D. H.; Thai, Y. T.; Nikles, D. E.; Brazel, C. S. Heating of Aqueous Dispersions Containing $MnFe_2O_4$ Nanoparticles by Radio-Frequency Magnetic Field Induction. *IEEE Trans. Magn.* **2009**, *45* (1), 64−70.

(16) Huang, H.; Delikanli, S.; Zeng, H.; Ferkey, D. M.; Pralle, A. Remote Control of Ion Channels and Neurons Through Magnetic-Field Heating of Nanoparticles. *Nat. Nanotechnol.* **2010**, *5* (8), 602−606.

(17) Na, H. B.; Song, I. C.; Hyeon, T. Inorganic Nanoparticles for MRI Contrast Agents. *Adv. Mater.* **2009**, *21* (21), 2133−2148.

(18) Lee, J.; Yang, J.; Seo, S.-B.; Ko, H.-J.; Suh, J.-S.; Huh, Y.-M.; Haam, S. Smart Nanoprobes for Ultrasensitive Detection of Breast Cancer via Magnetic Resonance Imaging. *Nanotechnology* **2008**, *19* (48), 485101.

(19) Lim, E.-K.; Yang, J.; Park, M.-y.; Park, J.; Suh, J.-S.; Yoon, H.-G.; Huh, Y.-M.; Haam, S. Synthesis of Water Soluble PEGylated Magnetic Complexes Using mPEG-Fatty Acid for Biomedical Applications. *Colloids Surf., B* **2008**, *64* (1), 111−117.

(20) Lee, T.; Lim, E.-K.; Lee, J.; Kang, B.; Choi, J.; Park, H. S.; Suh, J.-S.; Huh, Y.-M.; Haam, S. Efficient CD44-Targeted Magnetic Resonance Imaging (MRI) of Breast Cancer Cells Using Hyaluronic Acid (HA)-Modified $MnFe_2O_4$ Nanocrystals. *Nanoscale Res. Lett.* **2013**, *8* (1), 149.

(21) Sun, S.; Zeng, H.; Robinson, D. B.; Raoux, S.; Rice, P. M.; Wang, S. X.; Li, G. Monodisperse MFe_2O_4 (M = Fe, Co, Mn) Nanoparticles. *J. Am. Chem. Soc.* **2003**, *126* (1), 273−279.

(22) Bodini, M. E.; Willis, L. A.; Riechel, T. L.; Sawyer, D. T. Electrochemical and Spectroscopic Studies of Manganese(II), -(III), and -(IV) Gluconate Complexes. 1. Formulas and Oxidation-Reduction Stoichiometry. *Inorg. Chem.* **1976**, *15* (7), 1538−1543.

(23) Giri, A.; Goswami, N.; Pal, M.; Zar Myint, M. T.; Al-Harthi, S.; Singha, A.; Ghosh, B.; Dutta, J.; Pal, S. K. Rational Surface Modification of Mn_3O_4 Nanoparticles to Induce Multiple Photoluminescence and Room Temperature Ferromagnetism. *J. Mater. Chem. C* **2013**, *1* (9), 1885−1895.

(24) Takashima, T.; Hashimoto, K.; Nakamura, R. Mechanisms of pH-Dependent Activity for Water Oxidation to Molecular Oxygen by MnO_2 Electrocatalysts. *J. Am. Chem. Soc.* **2011**, *134* (3), 1519−1527.

(25) Huheey, J. E.; Keiter, E. A.; Keiter, R. L. *Inorganic Chemistry: Principles of Structure and Reactivity*, 4th ed.; Pearson Education: Singapore, 2006.

(26) Matzapetakis, M.; Karligiano, N.; Bino, A.; Dakanali, M.; Raptopoulou, C. P.; Tangoulis, V.; Terzis, A.; Giapintzakis, J.; Salifoglou, A. Manganese Citrate Chemistry: Syntheses, Spectroscopic Studies, and Structural Characterizations of Novel Mononuclear, Water-Soluble Manganese Citrate Complexes. *Inorg. Chem.* **2000**, *39* (18), 4044−4051.

(27) Aguado, F.; Rodriguez, F.; Núñez, P. Pressure-Induced Jahn-Teller Suppression and Simultaneous High-Spin to Low-Spin Transition in the Layered Perovskite $CsMnF_4$. *Phys. Rev. B: Condens. Matter Mater. Phys.* **2007**, *76* (9), 094417.
(28) Williams, A. T. R.; Winfield, S. A.; Miller, J. N. Relative Fluorescence Quantum Yields Using a Computer-Controlled Luminescence Spectrometer. *Analyst* **1983**, *108* (1290), 1067−1071.
(29) Giri, A.; Goswami, N.; Bootharaju, M. S.; Xavier, P. L.; John, R.; Thanh, N. T. K.; Pradeep, T.; Ghosh, B.; Raychaudhuri, A. K.; Pal, S. K. Emergence of Multicolor Photoluminescence in $La_{0.67}Sr_{0.33}MnO_3$ Nanoparticles. *J. Phys. Chem. C* **2012**, *116* (48), 25623−25629.
(30) Kaneko, N.; Kaneko, M.; Takahashi, H. Infrared and Raman Spectra and Vibrational Assignment of Some Metal Tartrates. *Spectrochim. Acta, Part A* **1984**, *40* (1), 33−42.
(31) Ramakrishnan, V.; Maroor, J. M. T. IR and Raman Studies of Gel Grown Manganese Tartrate. *Infrared Phys.* **1988**, *28* (4), 201−204.